arXiv:1106.2818v2 [cond-mat.supr-con] 4 Nov 2011

Disorder-dependent superconducting phase-diagram at high magnetic fields in $\mathbf{Fe}_{1+y}\mathbf{Se}_x\mathbf{Te}_{1-x}$ ($x \sim 0.4$)

T. Gebre,[1] G. Li,[1] J. B. Whalen,[1, 2] B. S. Conner,[1] H. D. Zhou,[1] G. Grissonanche,[1] M. K. Kostov,[1, 2] A. Gurevich,[1, 3] T. Siegrist,[1, 2] and L. Balicas[1, *]

[1] *National High Magnetic Field Laboratory, Florida State University, Tallahassee-FL 32310, USA*
[2] *Department of Chemical and Biomedical Engineering,*
Florida State University, Tallahassee-FL 32310, USA
[3] *Physics Department, Old Dominion University, Norfolk-VA 23529, USA*

(Dated: November 8, 2011)

We compare the superconducting phase-diagram under high magnetic fields (up to $H = 45$ T) of $\mathrm{Fe}_{1+y}\mathrm{Se}_{0.4}\mathrm{Te}_{0.6}$ single crystals originally grown by the Bridgman-Stockbarger (BRST) technique, which were annealed to display narrow superconducting transitions and the optimal transition temperature $T_c \gtrsim 14$ K, with the diagram for samples of similar stoichiometry grown by the traveling-solvent floating-zone technique as well as with the phase-diagram reported for crystals grown by a self-flux method. We find that the so-annealed samples tend to display higher ratios H_{c2}/T_c, particularly for fields applied along the inter-planar direction, where the upper critical field $H_{c2}(T)$ exhibits a pronounced downward curvature followed by saturation at lower temperatures T. This last observation is consistent with previous studies indicating that this system is Pauli limited. An analysis of our $H_{c2}(T)$ data using a multiband theory suggests the emergence of the Fulde-Ferrel-Larkin-Ovchnikov state at low temperatures. A detailed structural x-ray analysis, reveals no impurity phases but an appreciable degree of mosaicity in as-grown BRST single-crystals which remains unaffected by the annealing process. Energy-dispersive x-ray analysis showed that the annealed samples have a more homogeneous stoichiometric distribution of both Fe and Se with virtually the same content of interstitial Fe as the non-annealed ones. Thus, we conclude that the excess of Fe, in contrast to structural disorder, contributes to decrease the superconducting upper-critical fields of this series. Finally, a scaling analysis of the fluctuation conductivity in the superconducting critical regime, suggests that the superconducting fluctuations have a two-dimensional character in this system.

PACS numbers: 74.70.Xa, 74.25.Dw, 74.62.Dh, 74.25.fc

INTRODUCTION

The Fe_{1+y}(Te,Se) series is a quite unique superconducting system: its end member, FeSe is a superconductor with a superconducting transition temperature $T_c \simeq 8$ K, [1] which can be increased up to ~ 14 K with the partial substitution of Se for Te, [2, 3] or increased all the way up to 36.7 K by the application of hydrostatic pressure.[4] The other end member of this series $\mathrm{Fe}_{1+y}\mathrm{Te}$ is not superconducting and instead exhibits a simultaneous structural and magnetic phase transition from tetragonal to monoclinic lattice accompanied by antiferromagnetism (AFM) near $T_N \simeq 60$ to 70 K (Refs. 5–7). This AFM structure is distinct from those seen in the undoped FeAs based compounds.[8–10] The AFM order in $\mathrm{Fe}_{1+y}\mathrm{Te}$ propagates along the diagonal direction of the original undistorted Fe square lattice [5, 7], while in FeAs the wave-vector of the spin density wave (SDW) propagates along the nearest neighbor direction of the original Fe square lattice. [8–10]

Density functional theory (DFT) calculations indicate that the Fermi surfaces (FS) of both FeSe and FeTe are similar to those of the other FeAs based compounds, consequently they should satisfy the nesting condition for the wavevector $Q_{\pi,\pi} = (\pi, \pi)$. [11] This apparent lack of universality would seem to question the exclusive role of the interband pairing via $Q_{\pi,\pi}$ magnetic fluctuations in the pairing mechanism for all the iron-based superconductors. However, the observation of a spin resonance below T_c together with an enhancement of the spin fluctuations near it, indeed suggests a spin-fluctuations mediated superconducting pairing mechanism for this system.[12, 13] Initial angle resolved photoemission (ARPES) measurements in the $\mathrm{Fe}_{1+y}\mathrm{Te}$ revealed a pair of nearly compensated electron-hole FS pockets, with no evidence for the FS nesting instability associated with $Q_{\pi,\pi}$. [14] This could suggest the possibility of a distinct mechanism for the superconductivity and the magnetic-order in the Fe chalcogenides when compared to the Fe arsenides. But a recent ARPES study on superconducting $\mathrm{Fe}_{1.03}\mathrm{Te}_{0.7}\mathrm{Se}_{0.3}$ reveals a holelike and an electronlike FS located at the center and the corner of the Brillouin zone, respectively. These FSs are nearly nested for $Q_{\pi,\pi}$. [15] The same study reports an isotropic superconducting gap along the holelike FS with a gap Δ of ~ 4 meV ($2\Delta = k_B T_c \sim 7$), thus providing evidence for strong-coupling superconductivity. But, this is in contrast with a recent angle-dependent heat capacity study in $\mathrm{Fe}_{1+y}\mathrm{Se}_{0.45}\mathrm{Te}_{0.55}$ which finds evidence for a significant gap anisotropy on the electron pockets. [16] Superconductivity in $Fe_{1+y}Se$ was shown to be extremely sensitive to stoichiometry. [17] In the Fe_{1+y}(Te,Se) series, the crystal structure resembles that of the iron arsenides [1] with the Fe square planar sheets forming from the edge-sharing iron chalcogen tetrahedral network. But it also allows the partial occupation of iron in the interstitial sites of the (Te, Se) layers, resulting in a *nonstoichiometric* composition for the Fe_{1+y}(Te,Se) series, where y represents the excess Fe at the interstitial sites. [5, 6] It remains unclear how the geometry of the FS evolves with the incorporation of interstitial Fe, but it is claimed to suppress superconductivity. [18]

One remarkable feature of these compounds is their extremely large upper critical fields H_{c2}. For instance, according to Ref. 19 for a $Fe_{1.05}Te_{0.89}Se_{0.11}$ single-crystal with a middle point T_c of just 11 K, one observes an $H_{c2}(T \to 0\text{ K})$ of $\sim$ 35 T. Or for a single-crystal of $Fe_{1.11}Te_{0.6}Se_{0.4}$ with a T_c close to its optimum value of 14 K one obtains $H_{c2}(T \to 0\text{ K})$ of $\sim$ 40 to 45 T. [20] Compare these values with those of, for instance, MgB_2 single crystals: $T_c = 39$ K with $H^c_{c2}(0) = 3.5$ T and $H^{ab}_{c2}(0) = 17$ T, for fields along the c-axis and along a planar direction, respectively. [21] In fact, to achieve in MgB_2 upper-critical fields as large as those observed in the Fe_{1+y}(Te,Se) series, strong impurity scattering is introduced to optimize the relative strengths of intraband scattering in σ and π bands of MgB_2. [22, 23] The significant differences between these two multi-band superconducting families are attributable to the fact that the Fe_{1+y}(Te,Se) superconductors are mostly Pauli limited [19] while the H_{c2}s in MgB_2 are mostly determined by the orbital pair-breaking effect. However, the shape of the $H_{c2}(T)$ curves for Fe_{1+y}(Te,Se) series measured in Refs. 20 and 19 are quite distinct, with the former presenting a nearly linear dependence of $H_{c2}(T)$ for $\mathbf{H}\|c$ and the second displaying a pronounced concave down curvature followed by saturation at lower temperatures (as expected for the Pauli limiting effect). Such a curvature has also been reported in Ref. 24.

The Pauli-limited behavior of $H_{c2}(T)$ for Fe-chalcogenides results from the fact that they are semimetals with rather low carrier density and low Fermi energies $\sim 20-50$ meV for different FS pockets [14, 15], unlike the conventional metallic superconductor MgB_2. As a result, chalcogenides have very short coherence lengths $\xi_0 \simeq \hbar v_F/2\pi T_c < 1$ nm and thus extremely high orbitally-limited $H^{orb}_{c2} \sim \phi_0/2\pi\xi^2$ where v_F is the Fermi velocity in the ab plane, and ϕ_0 is the flux quantum. This in turn greatly enhances the Pauli effects quantified by the Maki parameter $\alpha_M = \sqrt{2}H^{orb}_{c2}/H_p$ where $H_p[T] = 1.84T_c[K]$ is the Clogston paramagnetic limit [25]. Chalcogenides typically have $\alpha_M \gtrsim 1$ above the critical value at which the FFLO instability develops. Moreover, because of their very short values of ξ_0, chalcogenides are naturally in the clean limit $\ell \gg \xi_0$ which is one of the conditions of the FFLO instability, where ℓ is the mean free path due to elastic impurity scattering [25]. These features of chalcogenides make them good candidates to study exotic effects at high magnetic fields, in particular, the interplay of orbital and paramagnetic pairbreaking for multiband pairing and the FFLO state at low temperatures. The small Fermi energies also make superconducting properties very sensitive to the doping level, allowing one to tune H_{c2} by small shifts of the chemical potential.

In contrast to other reports emphasizing on the details concerning the synthesis of single crystals [26], in this work we compare the high-field phase-diagram of the Fe_{1+y}(Te,Se) series, particularly the diagram for the optimally doped compound $Fe_{1+y}Te_{1-x\approx0.6}Se_{x\approx0.4}$ synthesized by two methods. The first one is based on a traveling-solvent floating zone growth technique (TSFZ), which leads to crystals of acceptable crystallinity displaying “non-metallic” resistivity, optimal T_cs, and transition widths $\Delta T_c \simeq 1$ to 3 K. We compare their behavior with crystals resulting from the Bridgman-Stockbarger (BRST) technique which in our case leads to crystals of poorer crystallinity (i.e. larger mosaicity), wider transitions and frequently to non-optimal T_cs in as grown crystals, as previously reported by other groups. [27] These last single-crystals were subjected to an annealing procedure which lead to metallic resistivity, considerably sharper resistive transitions $\Delta T_c \simeq 1$ K, and to superconducting transitions comparable to those reported in the literature for high quality BRST-grown single crystals as measured by SQUID magnetometry. [28] The annealed crystals having a clear metallic behavior preceding superconductivity, display considerably higher upper-critical fields when compared to those showing a poor metallicity, particularly for magnetic-fields applied along the inter-layer direction. This increase leads to a distinct shape of the $H^c_{c2}(T)$, i.e. from a approximately linear in T behavior as reported in Ref. 20, to the marked concave-down curvature followed by saturation at lower temperatures as seen in Ref. 24.The analysis of our experimental data using a multiband theory of $H_{c2}(T)$ [29] shows that $H_{c2}(T)$ is indeed strongly Pauli limited $\alpha_M \simeq 7-10$, predicting the FFLO state below ≈ 5 K. A detailed single crystal x-ray analysis reveals that the annealing process does not affect the crystallinity or the degree of mosaicity of our single crystals. Nevertheless, our dispersive x-ray analysis indicates that the annealing process leads to a more uniform distribution of interstitial Fe. Annealing yields a considerably more isotropic phase diagram which combined with the enhancement in $H^c_{c2}(T)$, suggests that the variations in the content of interstitial Fe contributes to the suppression of superconductivity. Finally, we show, through a scaling analysis of the fluctuation conductivity in the neighborhood of the superconducting transition, that the superconducting fluctuations in this system are two-dimensional in character.

SAMPLE PREPARATION

Single crystals of $Fe_{1+x}Te_{1-y}Se_y$, $0.05 \leq x \leq 1$ and $0.1 \leq y \leq 0.5$ were grown by using the traveling-solvent floating-zone growth technique (TSFZ) and the Bridgman-Stockbarger (BRST) techniques. Starting materials with nominal purities of 4N for Fe and 5N for Te and Se were used. These were handled in an argon-filled glove box which kept the oxygen content below 1ppm. Mixtures of Fe, Te, and Se were ground and pelletized and sealed in quartz ampoules under vacuum and heated at 400 °C for 24 h. The reacted material was reground and doubly sealed in two quartz ampoules. For samples grown through the TSFZ technique, the doubly sealed quartz ampoules were loaded into an optical floating-zone furnace (NEC Nichiden Machinery 15HD), equipped with two 1500 W halogen lamps. The ampoule was rotated at 20 rpm, and translated at a rate of 1 to 2 mm/h. The as-grown samples were annealed by heating to 800 °C for 48 h, and then cooled at a rate of 100 °C/h to 420 °C and held at this temperature for additional 30 h, followed by the cooling of the furnace to room temperature.

A double wall quartz ampoule was also used in the case of crystals grown by the BRST technique. The inner ampoule was narrowly tipped at its bottom and sealed at the top. This Bridgman ampoule was inserting into a three-zone temperature gradient vertical furnace and lowered at a speed of 4 mm/h. The growth temperature was decreased at a rate of 3 °C/h down to 440 °C and subsequently quenched to room temperature. Some of the crystals as well as Se powder were placed into two different quartz crucibles, and both placed inside an evacuated quartz ampoule which was sealed under vacuum and heated slowly to 400 °C and then annealed for ten days.

The so-obtained crystals were checked by both single-crystal and powder x-ray diffraction (XRD) techniques. From as-grown single crystals, shards were cleaved to obtain suitable samples of approximately 0.3 mm × 0.3 mm × 0.03 mm. An Oxford-Diffraction Xcalibur-2 CCD diffractometer with Mo K_α source was used to collect reflections. CrysAlis Pro 171.33.55 software (Oxford Diffraction) was used for the unit cell refinement and analytical absorption correction. Final structure refinements were conducted using SHELXTL. For the powder diffraction runs, the single-crystals were ground by hand for approximately 1 minute using an agate mortar and pestle. Patterns were detected by a Huber-Guinier 620 camera with a Rigaku Ultrax Cu K_α direct drive rotating anode source. WinPow software was used for unit cell parameter least-squares calculations and peak fitting. Further details are provided in Ref. 30.

Scanning electron-microscope energy-dispersive x-ray analysis (SEM-EDX) was performed by using a JEOL 5900 scanning electron microscope (30 kV accelerating voltage) equipped with IXRF energy dispersion spectroscopy software (IXRF Systems, Inc.) in order to determine the elemental compositions of the single crystals. We found that this EDX set-up would show a tendency to underestimate by nearly 3 % the overall fraction of Fe when comparing with detailed single-crystal x-ray refinements. We must clarify that the EDX set-up was not calibrated against an absolute standard.

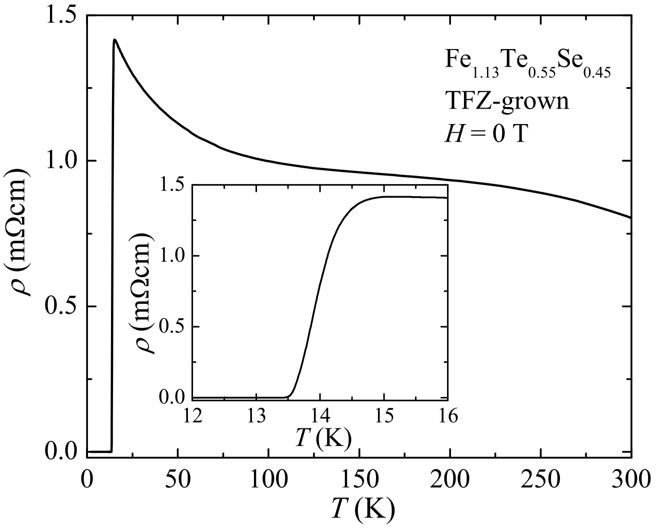

FIG. 1. (color online) Top panel: Resistivity as a function of temperature for a $Fe_{1.13}Se_{0.45}Te_{0.55}$ single crystal synthesized by the traveling floating zone method under zero magnetic field. Inset: Resistive superconducting transition under zero-field in a limited temperature range.

Longitudinal resistivity was measured using a conventional four-contact method in continuous magnetic fields up to 45 T by using either a PPMS or the hybrid magnet of the National High Magnetic Field Laboratory in Tallahassee.

SAMPLE CHARACTERIZATION

Figure 1 shows a typical trace of resistivity ρ as a function of the temperature for a single crystal grown by the traveling-solvent floating-zone method described above, whose stoichiometry was extracted by a detailed single crystal x-ray analysis refinement. Although the width $\Delta T_c \sim 1$ K of the superconducting transition (see inset) is relatively narrow when compared with the width of the transitions shown for instance in Ref. [19], the behavior of the metallic state shows the typical negative slope $\partial\rho/\partial T < 0$ or logarithmic divergence of the resistivity, which was attributed to the high content of interstitial Fe and which leads to weak localization. [18] The same characteristic temperature dependent resistive behavior is observed also in as-grown samples synthesized by the Bridgman-Stockbarger method (red line), as seen

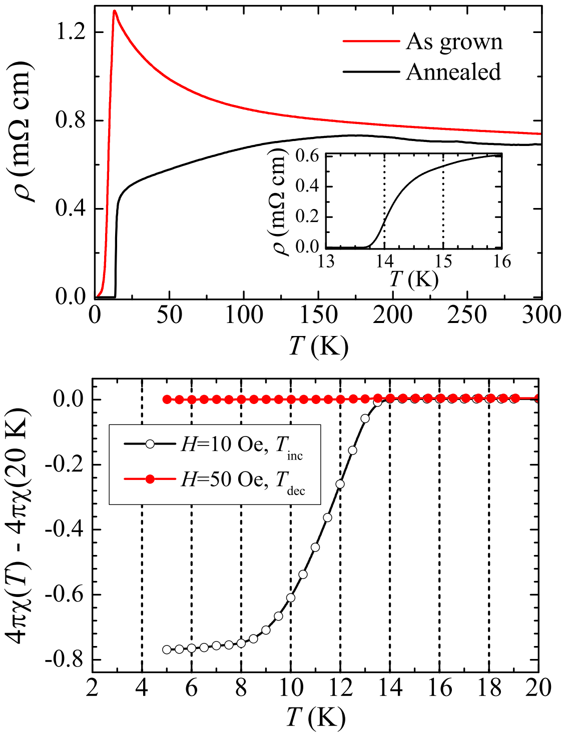

FIG. 2. (color online) Top panel: Resistivity as a function of temperature for an as-grown $Fe_{1.11}Se_{0.4}Te_{0.6}$ single crystal, synthesized through the Bridgman-Stockbarger method (red curve) and under zero magnetic field. After annealing, the sample no longer displays the weak-localization like temperature dependence. Instead it displays a metallic character (black trace). Inset: Superconducting resistive transition for the annealed crystal under zero field and in a limited temperature range. Bottom panel: Magnetic susceptibility as a function of T for the same annealed single-crystal and respectively, for magnetic field-cooled (red markers) and zero-field cooled conditions (black markers).

in the top panel of Fig. 2. As seen, the as-grown samples tend to exhibit lower superconducting transition temperatures and broader transitions. The annealing procedure described above leads to a slightly smaller resistivity at room temperature (black line) but most importantly to a quite distinct temperature dependence for the resistivity, which below $T \sim 175$ K exhibits a clear metallic dependence with $\partial\rho/\partial T > 0$. The magnetic susceptibility on the other hand, shows a very clear diamagnetic signal (black markers) below the onset of T_c at $T = 14$ K, as seen in the lower panel of Fig. 2. At higher temperatures, the magnetic susceptibility is virtually temperature independent, as reported in Ref. 31 , and only at low temperatures one observes a very mild upturn in the susceptibility suggesting the presence of a small amount of localized magnetic moments. Although none of the susceptibility traces in Ref. 31 show a clear diamagnetic signal below $T_c \simeq 14$ K but below ~ 10 K.

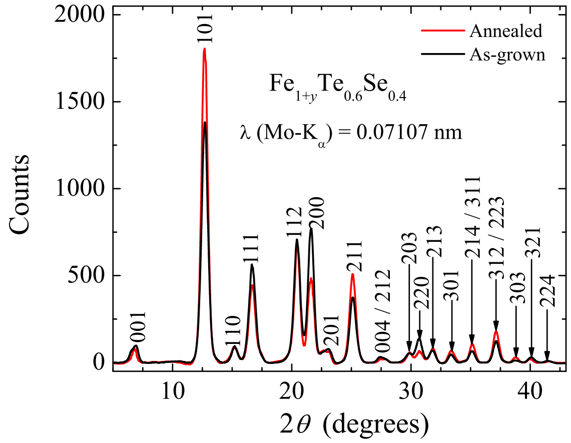

FIG. 3. (color online) Powder x-ray diffraction pattern for two $Fe_{1.11}Se_{0.4}Te_{0.6}$ single crystals grown through the Bridgman technique, collected by using the Mo-K$_\alpha$ line. Black line corresponds to the spectrum of an as-grown crystal, while the red line is the spectrum obtained from a subsequently annealed single-crystal. In both cases well-defined Bragg peaks are observed and indexed within the space-group $P4/nmm$. We find no evidence for impurity phases or a change in structure/stoichiometry induced by the annealing process.

We also characterized our single crystals through single-crystal and powder x-ray diffraction measurements. Figure 3 shows two typical powder x-ray spectrum for one *as-grown* BRST crystal (black line) with a nominal stoichiometry $Fe_{1.11}Se_{0.4}Te_{0.6}$, and for one *annealed* BRST single crystal (red line) from the same batch. These "powder" patterns were produced from integrating the intensities from single-crystal x-ray diffraction measurements using an area detector. This powder like pattern was obtained on the same single crystals used for the magnetic and transport measurements shown throughout this manuscript, by superimposing several of the θ to 2θ scans along the different crystallographic orientations. As clearly seen, for both crystals we observe the same set of well-defined Bragg peaks, where all peaks can be indexed within the tetragonal unit cell having the space group symmetry $P4/nmm$. Most importantly, we do not detect the presence of any impurity phase in either crystal, concluding that the annealing process preserves the original crystallographic structure and therefore the stoichiometry of the crystals. From this first analysis it would seem that both crystals are equivalent in structural quality despite their marked differences in physical behavior as seen in the top panel of Fig. 2.

To clarify if disorder and mosaicity is at the origin of these differences in physical behavior, we performed a detailed x-ray rocking curve analysis in both single crystals around specific Bragg peaks. Figure 4 (a) shows the

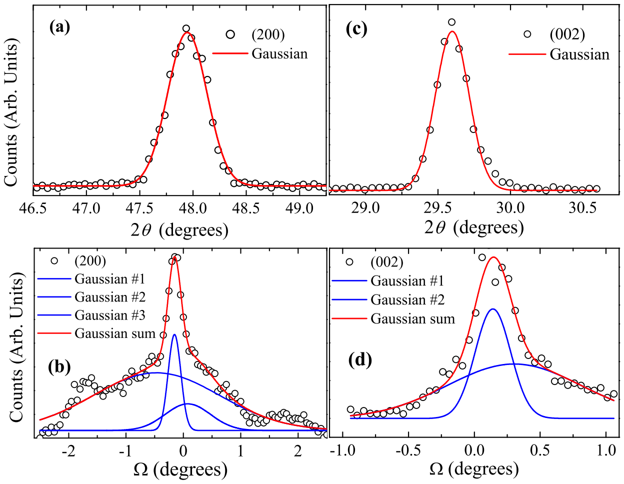

FIG. 4. (color online) (a) X-ray intensity for an as-grown BS single-crystal as a function of 2θ for an angular scan around the Bragg-peak observed along the real-space direction (abc) = (200). Red line is a fit to a Gaussian function which yields a full-width at half-maximum of $\sim 0.5^\circ$. (b) X-ray rocking curve around the Bragg peak at (200) as a function of the angle Ω, which corresponds to an arc along a direction nearly perpendicular to θ. One observes a very broad feature which can be adjusted to three Gaussian distributions (blue lines) of crystallite orientations. (c) Same as in (a) but for a Bragg peak centered at the (002) position. Red line is a fit to a Gaussian having a full-width at half-maximum of $\sim 0.25^\circ$. (d) Same as in (b) but for the peak around the (002) position, although in this case two Gaussian distributions are needed to adjust the observed broad peak.

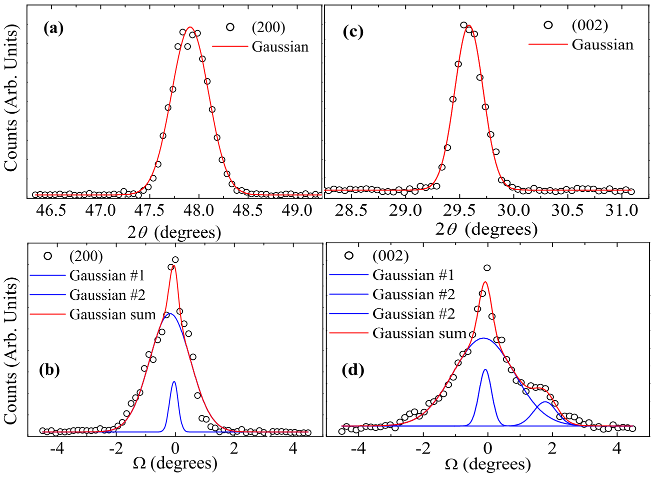

FIG. 5. (color online) (a) X-ray intensity for an *annealed* BRST single-crystal of $\mathrm{Fe}_{1+y}\mathrm{Te}_{0.6}\mathrm{Se}_{0.4}$ as a function of 2θ for an angular scan around the Bragg-peak observed along the real-space position $[abc]$ = (200). Red line is a fit to a Gaussian function which yields a width at half maximum of $\sim 0.4^\circ$. (b) X-ray rocking curve around the Bragg peak at (200) as a function of the angle Ω. One observes a very broad feature which can be adjusted to at least two Gaussian distributions (blue lines) of crystallite orientations. (c) Same as in (a) but for a Bragg peak observed along (002) position. Red line is a fit to a Gaussian which yields a full width at half-maximum of $\sim 0.3^\circ$. (d) Same as in (b) but for the peak around the (002) position.

(200) Bragg reflection. By fitting the intensity as a function of 2θ to a Gaussian distribution, one obtains a full width at half maximum (FWHM) of $\sim 0.5^\circ$, suggesting at first glance a modest but sizeable mosaic spread among crystallites. However, an exploration of the width of this peak along an arc Ω whose orientation is nearly perpendicular to 2θ reveals a very broad feature as seen in Fig. 4 (b). This broad maximum can be adjusted (red line) to 3 Gaussian distributions (blue lines), with one of them showing a FWHM as large as $\gtrsim 2.5^\circ$. Each Gaussian would represent an ensemble or distribution of crystallites having a similar relative orientation. The observation of several distributions with varying widths indicates a large degree of mosaicity around the (200) position, or within the planes. A similar study around the (002) position shown respectively in Figs. 4 (c) and 4 (d), reveals seemingly a smaller degree of mosaicity among crystallites within distinct planes.

To clarify if the annealing process affects the structural degrees of freedom, for instance, by releasing strain induced in the single-crystals by the synthesis process, we have attempted a similar detailed structural analysis in an annealed single crystal of $\mathrm{Fe}_{1+y}\mathrm{Te}_{0.6}\mathrm{Se}_{0.4}$. Figure 5 (a) shows the intensity of the Bragg peak located along the (200) direction as a function of the angle 2θ, while Fig. 5 (b) shows the intensity of the same peak as function of the angle Ω. The first measurement leads to a Gaussian peak (red line) having a FWHM of $\simeq 0.4^\circ$ while the second one can be adjusted to two Gaussian distributions (blue lines) with the widest distribution having a FWHM of $\simeq 1.6^\circ$. Fig. 5 (c) shows the intensity of the Bragg peak observed as the angle 2θ is scanned around the (002) direction. One extracts a FWHM of $\simeq 0.3^\circ$ by fitting its intensity to a Gaussian distribution (red line). Finally, Fig. 5 (d) shows the intensity of the Bragg peak observed at the (002) position as a function of the angle Ω. As shown in the figure, to reproduce the observed broad feature one would need to fit it to at least three Gaussian distributions with the widest one having a FWHM of $\gtrsim 2.1^\circ$.

From this detailed comparison between the as-grown and the annealed BRST $\mathrm{Fe}_{1+y}\mathrm{Te}_{0.6}\mathrm{Se}_{0.4}$ single crystals, we can firmly conclude that the annealing process has no or perhaps just a marginal effect on the degree of crystallinity of the BRST grown samples. Although as seen in Fig. 2 (a), the behavior of the metallic state, and even the width of the superconducting transition is affected by this treatment and as we shall see below, it also affects $H_{c2}(T)$. In Figs. 6 (a) through (d) we show a similar rocking curve analysis for a typical TSFZ

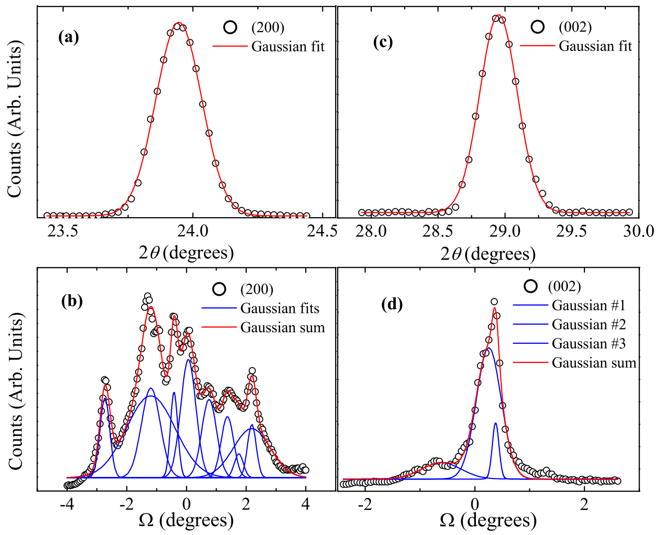

FIG. 6. (color online) (a) X-ray intensity for a single-crystal of $Fe_{1+y}Te_{0.55}Se_{0.45}$ grown by the traveling floating zone method as a function of 2θ for an angular scan around the Bragg-peak observed along the (200) position. Red line is a fit to a Gaussian function which yields a width at half maximum of $\sim 0.2^\circ$. (b) X-ray rocking curve around the Bragg peak at (200) as a function of the angle Ω. One observes a very broad feature which can be adjusted to a superposition of least ten Gaussian distributions (blue lines) of crystallite orientations. (b) Same as in (a) but for a Bragg peak observed along (002) position. Red line is a fit to a Gaussian which yields a full width at half-maximum of $\sim 0.3^\circ$. (d) Same as in (b) but for the peak around the (002) position.

$Fe_{1+y}Te_{0.55}Se_{0.45}$ single-crystal, and as can clearly be seen in Figs. 6 (b) and (c) the degree of mosaicity in this single crystal, is higher (spans over 6°) than what we found for the BRST crystals. Nevertheless, the width of the superconducting transition (see Fig. 1) is considerably sharper than the width of the transition in as grown BRST crystals (see Fig. 2(a)) Therefore, from our study we can state that the mosaicity, or the relative orientation between stacked planes in a single-crystal, has virtually no effect on the superconducting properties (such as the width of the transition) of the 11 series.

Nevertheless, by comparing the EDX data taken on several annealed and non-annealed BRST-grown single-crystals, on approximately a dozen of collection sites in each crystal, one notices marked differences between annealed and non-annealed crystals: in average the non-annealed crystals displayed a variability Δy of ~ 7.7 % in the fraction y of interstitial Fe and a $\Delta x \simeq 8.8$ % in the fraction x of Se, when compared respectively to $\Delta y = 1.8$ % and $\Delta x = 6.1$ % for the annealed samples (Δy is the average of the fluctuations with respect to the average value of y). EDX indicates that the annealing process has virtually no effect on the average value of either x or y, so it just homogenizes both values (specially y) throughout the sample.

However, this observation does not address the origin of for instance, the "non-metallic" like resistivity observed in the TSFZ-grown crystals when compared to the metallic response seen in annealed BRST-grown crystals. For the first ones, we were able to observe clear Bragg peaks and proceed with single-crystal x-ray refinements in shards taken from them, indicating relatively large values for y ranging from 0.07 to 0.12. The crystallographic information file for one of our single-crystals is available as supplemental material [32]. We also performed EDX analysis on the TSFZ single crystals, finding similar amounts of excess interstitial Fe, and typical values for $\Delta y \simeq 2$ %. Remarkably, for the second ones and despite the physical characterization shown above suggesting relatively high-quality single-crystals, we were unable to extract well-defined integrated intensities to proceed with single-crystal x-ray refinements. For these crystals, EDX indicates nearly stoichiometric values for y, i.e. $y \sim 0$ although, as previously mentioned, it tends to underestimate the content of Fe when compared to single-crystal x-ray refinements. These observations indicate that the physical properties of the 11 Fe-chalcogenides are nearly oblivious to their degree of mosaicity but depend on the amount of interstitial Fe and on how evenly distributed it is throughout the sample.

SUPERCONDUCTING PHASE DIAGRAM AT HIGH FIELDS

In this section we compare the high-field superconducting phase-diagrams of several crystals synthesized by either the floating zone or the Bridgman-Stockbarger technique. In each case, only the crystals displaying the sharpest superconducting transitions $\Delta T_c = T(\rho(0.9T_c) - T(\rho(0.1T_c)) \lesssim 1.0$ K (where $\rho(0.9T_c)$ and $\rho(0.1T_c)$ are the values of the resistivity at respectively, the onset of the resistive transition or 90 % of ρ, and the foot or 10 % of ρ at the transition) were chosen for the electrical transport measurements under high fields. As indicated by Fig. 2, for the crystals grown by BRST the method, only the annealed samples showed the optimum T_c and the sharpest superconducting transitions among all of the measured samples.

Figures 7 (a) and (b) show the resistance as a function of temperature for an annealed $Fe_{1+y}Te_{0.6}Se_{0.4}$ single crystal for different fields $\mathbf{H} \| ab$ and $\mathbf{H} \| c$, respectively. Clearly, fields along the c-axis produce broader transitions as a function of temperature. Figures 7 (c) and (d) show the resistance as a function of magnetic fields $\mathbf{H} \| ab$ and $\mathbf{H} \| c$ (up to $H = 45$ T) for the same single crystal for different temperatures. The transitions become progressively sharper in field as the temperature decreases, consistent with the reduction of vortex fluctuations at lower T. We have also collected similar data-sets for several

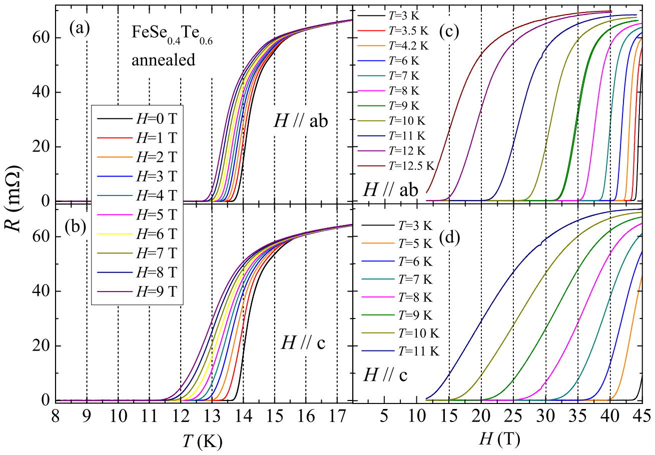

FIG. 7. (color online) Left panel: Resistance as a function of temperature T across the superconducting transition for an annealed $Fe_{1.11}Se_{0.4}Te_{0.6}$ single crystal (nominal stoichiometry) synthesized by the Bridgeman technique, and respectively for fields along an in-plane direction (a) and the inter-plane c-axis (b). Right panel: Resistance as a function of field H for the same single-crystal and for different temperatures, and respectively for an in-plane direction (c) and the inter-plane c-axis (d).

single-crystals grown by the TSFZ-method with different Se and Fe contents but the corresponding raw data is not shown here. The stoichiometric fractions of Fe and Se were determined through a detailed single-crystal x-ray diffraction refinement of small shards cleaved off from each single-crystal. For these TSFZ samples the measured superconducting transition temperatures ranged from $T_c \sim 12$ K ($y = 0.26$, x or fraction of Se $= 0.16$) to the optimal T_c value $\gtrsim 14$ K ($y = 0.06$ and $x = 0.44$).

In Fig. 8 (a) we compare the superconducting phase-diagram at high-fields for our annealed BRST $Fe_{1+y}Te_{0.6}Se_{0.4}$ single-crystal (circles) with the results of Ref. 20 (squares), and in Fig. 8 (b) with the phase-diagram obtained for several TSFZ single-crystals (various markers excluding circles). Here, all points correspond to the middle point of the resistive transition. In either graph, both the field- and the temperature-axis are re-scaled with the zero-field T_c of each sample (corresponding to the middle point of the zero-field resistive transition). Here, we use this scaling for comparative purposes only, and not to indicate that these compounds are placed within the dirty limit. The plot in Fig. 7 (a) leads to a similar scaling quality when compared with a $H_{c2}(T)/T_c^2$ as a function of T/T_c plot, previously observed in some of the Fe arsenide compounds [35] and which was deemed to be consistent with an effective clean limit scenario due to the small superconducting coherence lengths of the Fe-pnictide compounds. As clearly seen in both figures, the annealed BRST-grown crystal has considerably larger upper-critical fields than all the other crystals, particularly for fields along the c-axis and at intermediary reduced temperatures, i.e. from ~ 35 to ~ 60 % larger H_{c2}s for $T/T_c \simeq 0.5$. For $T/T_c \simeq 0.2$, the upper-critical field still is ~ 5 % larger than the value reported in Ref. 20. On the other hand, the anisotropy parameter $\gamma \simeq 1.8$ for $T \to T_c$ is slightly smaller than the values reported in Ref. 20 ($\gamma \simeq 2$ for $T \to T_c$), Ref. 24 ($\gamma \simeq 3$ for $T \to T_c$), and Ref. 33 ($\gamma \simeq 3.5-4$ for $T \to T_c$). Given that the level of structural disorder (i.e. mosaicity) seen in crystals showing quite broad transitions and lower T_cs (as-grown BRST crystals) is very similar to the level of mosaicity seen in the annealed crystals which display relatively sharp transitions, optimum T_c, and higher H_{c2}, one is lead to conclude that the superconducting phase diagram of the $Fe_{1+y}Te_{1-x}Se_x$ series for a given value of x is mostly controlled by Δy and Δx respectively the overall fluctuation on the value of y the fraction of interstitial Fe and in the value of x the fraction of Se.

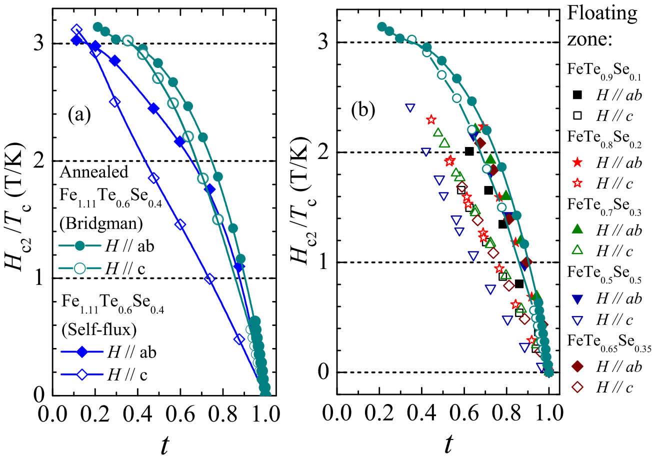

FIG. 8. (color online) (a) Comparative superconducting phase-diagram under high magnetic fields where the upper critical field H_{c2} normalized by the superconducting transition temperature T_c, is plotted as a function of the reduced temperature $t = T/T_c$ for two single crystals: respectively for the $Fe_{1+\delta}Se_{0.4}Te_{0.6}$ single crystal in Ref. 20 and for our annealed $Fe_{1.11}Se_{0.4}Te_{0.6}$ (nominal stoichiometry) BRST single-crystal. (b) Superconducting phase-diagram for several TSFZ grown single-crystals, where the phase-diagram for our annealed $Fe_{1.11}Se_{0.4}Te_{0.6}$ BRST single-crystal is also included. Open and solid markers depict the phase-boundary between metallic and superconducting states for fields along the c-axis and along a planar direction, respectively. All points in both graphs were extracted from the middle point of the resistive transition.

Another intriguing observation is that the superconducting phase-diagram for the more Fe stoichiometric samples shows a pronounced downward curvature as T is lowered which was attributed by several authors to the Pauli limiting effect [19, 33], in contrast with for example, the linear dependence seen in Ref. 20) for H_{c2}^c. Indeed, all $H_{c2}/T_c \simeq 3$ ratios shown in Fig. 7 are above the BCS

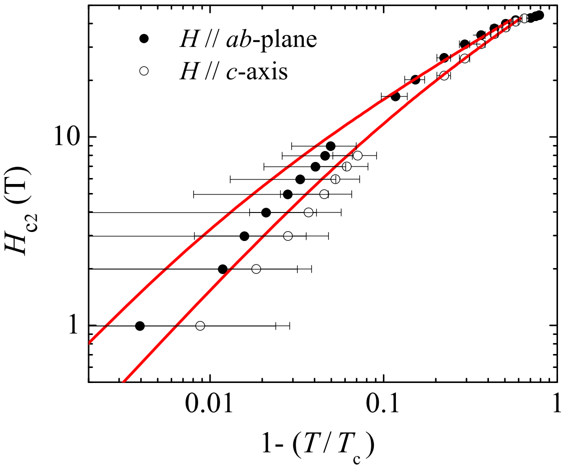

FIG. 9. (color online) Upper critical fields H_{c2} as a function of $1-t$ where $t = T/T_c$ is the reduced temperature for an annealed Bridgman-Stockbarger grown single-crystal. Red lines are fits to Eq. 1. It yields values for the coherence lengths ξ_{ab} and ξ_c which are in good agreement with those of Ref. 33.

paramagnetic limit, $H_{c2}/T_c = 1.84$, indicating that the Pauli pairbreaking is very essential.

Two-band analysis of the H_{c2} data

In order to evaluate the contributions of both orbital and Pauli pairbreaking effects for either field orientation, and to compare the results with those extracted from heat capacity measurements, we first analyze our $H_{c2}(T)$ data at temperatures close to T_c where the Ginzburg-Landau theory yields Ref. [29, 33]:

$$\left(\frac{H}{H_p}\right)^2 + \frac{H}{H_\mathrm{o}} = 1 - \frac{T}{T_c} \tag{1}$$

Very close to the critical temperature, $(T_c - T)/T_c \ll (H_p/H_\mathrm{o})^2$, the first paramagnetic term in the left hand side is negligible and Eq. (1) yields the orbital linear GL temperature dependence, $H_{c2} = H_\mathrm{o}(1 - T/T_c)$. At lower temperatures, $(T_c - T)/T_c > (H_p/H_\mathrm{o})^2$, the Pauli limiting field H_p dominates the shape of $H_{c2}(T) \propto (1-t)^{1/2}$ even in the GL domain if $H_p < H_\mathrm{o}$. The latter inequality is equivalent to the condition that the Maki parameter $\alpha_M \sim H_\mathrm{o}/H_p > 1$ is large enough, assuring that the paramagnetic effects are essential. Shown in Fig. 9 are the log-log plot of our $H_{c2}(T)$ as a function of $1 - T/T_c$ where the red lines are fits to Eq. (1). These fits are excellent for the high-field region (excluding the highest fields), but less so very close to T_c, probably due to the relatively large errors in determining temperatures ($\Delta T \sim 25$ mK) which are inherent to transport measurements, or perhaps due to broadening of the resistive transition due to local T_c inhomogeneities. The fit yields $H_p^{\|c} = (72.3 \pm 3.5)$ T and $H_p^{\|ab} = (62.6 \pm 2.4)$ T for the Pauli limiting field, respectively for fields along the c-axis and along the ab-plane, and $H_\mathrm{o}^{\|c} = (160.1 \pm 17.3)$ T and $H_\mathrm{o}^{\|ab} = (439 \pm 136)$ T for the orbital limiting fields which are in very good agreement with those reported in Ref. 33. Defining the effective GL coherence lengths, $\xi_{ab}(T) = \xi_{ab}(1 - T/T_c)^{-1/2}$ and $\xi_c(T) = \xi_c(1 - T/T_c)^{-1/2}$, we obtain a rather small in-plane value of $\xi_{ab} = (\phi_0/2\pi H_\mathrm{o}^{\|c})^{1/2} = 14 \pm 4$ Å and an even smaller c-axis value of $\xi_c = \xi_{ab} H_\mathrm{o}^{\|c}/H_\mathrm{o}^{\|ab} \sim 5.1$ Å, which is shorter than the inter-planar distance $c \sim 6$ Å [34], in agreement with Ref. 33.

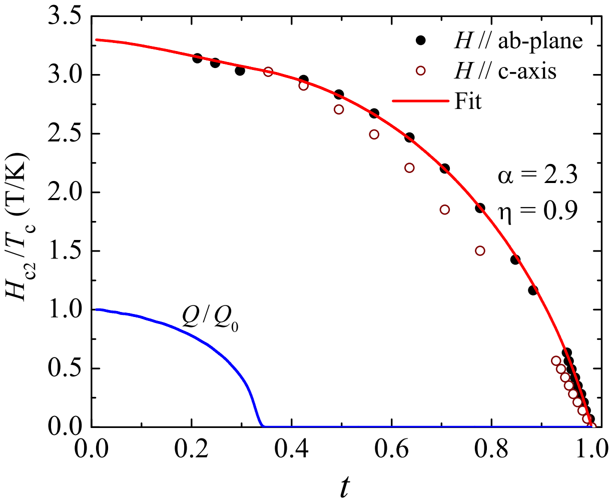

FIG. 10. (color online) High-field superconducting phase-diagram or upper critical-field normalized by the superconducting transition temperature at zero field as function of the reduced temperature, for an annealed BRST-grown $\mathrm{Fe}_{1+\delta}\mathrm{Se}_{0.4}\mathrm{Te}_{0.6}$ single crystal, where the red line is a fit to the model described in the text. Blue line depicts the temperature dependence of the modulation wave-vector for a FFLO state, which would explain the shape of the phase-boundary at lower temperatures.

The phenomenological Eq. (1) only describes the range $T \approx T_c$, but does not take into account the possibility of the FFLO state which occurs if $\alpha_M > \alpha_c$ is large enough ($\alpha_c \approx 1.8$ for a single parabolic band [25]). To analyze our $H_{c2}(T)$ data at all temperatures and to reveal the microscopic meaning of the scaling fields H_p and H_o, we use a two-band generalization of the WHH theory [29] in the clean limit, taking into account both orbital and paramagnetic pair-breaking, and the possibility of the FFLO with the wave vector $Q(T, H)$. In this case the equation for H_{c2} is given by

$$a_1G_1+a_2G_2+G_1G_2=0, \tag{2}$$

$$G_1=\ln t+2e^{q^2}\,\mathrm{Re}\sum_{n=0}^{\infty}\int_q^{\infty}du e^{-u^2}\times$$
$$\left[\frac{u}{n+1/2}-\frac{t}{\sqrt{b}}\tan^{-1}\left(\frac{u\sqrt{b}}{t(n+1/2)+i\alpha b}\right)\right]G_2=$$
$$\ln t+2e^{sq^2}\,\mathrm{Re}\sum_{n=0}^{\infty}\int_{q\sqrt{s}}^{\infty}du e^{-u^2}\times$$
$$\left[\frac{u}{n+1/2}-\frac{t}{\sqrt{b\eta}}\tan^{-1}\left(\frac{u\sqrt{b\eta}}{t(n+1/2)+i\alpha b}\right)\right] \tag{3}$$

The FFLO wave vector $Q(T,H)$ is determined self-consistently by the condition that the solution $H_{c2}(T,Q)$ of Eq. (2) is maximum, $a_1=(\lambda_0+\lambda_-)/2w$, $a_2=(\lambda_0-\lambda_-)/2w$, $\lambda_-=\lambda_{11}-\lambda_{22}$, $\lambda_0=(\lambda_-^2+4\lambda_{12}\lambda_{21})^{1/2}$, $w=\lambda_{11}\lambda_{22}-\lambda_{12}\lambda_{21}$, $t=T/T_c$, and

$$b=\frac{\hbar^2v_1^2H}{8\pi\phi_0k_B^2T_c^2g_1^2},\qquad \alpha=\frac{4\mu\phi_0g_1k_BT_c}{\hbar^2v_1^2}=\frac{\pi k_BT_cm}{E_Fm_0}, \tag{4}$$

$$q^2=Q_z^2\phi_0\epsilon_1/2\pi H,\qquad \eta=v_2^2/v_1^2,\qquad s=\epsilon_2/\epsilon_1. \tag{5}$$

Here v_l is the in-plane Fermi velocity in band $l=1,2$, $\epsilon_l=m_l^{ab}/m_l^c$ is the mass anisotropy ratio, μ is the magnetic moment of a quasiparticle, λ_{11} and λ_{22} are the intraband pairing constants, and λ_{12} and λ_{21} are the interband pairing constants, and $\alpha\approx 0.56\alpha_M$. The factors $g_1=1+\lambda_{11}+|\lambda_{12}|$ and $g_2=1+\lambda_{22}+|\lambda_{21}|$ describe the strong coupling Eliashberg corrections. For the sake of simplicity, we consider here the case of $\epsilon_1=\epsilon_2=\epsilon$ for which $s=1$, and H_{ab} is defined by Eqs. (2) and (3) with $g_1=g_2$ and rescaled $q\to q\epsilon^{-3/4}$, $\alpha\to\alpha\epsilon^{-1/2}$ and $\sqrt{b}\to\epsilon^{1/4}\sqrt{b}$ in G_1 and $\sqrt{\eta b}\to\epsilon^{1/4}\sqrt{\eta b}$ in G_2 [29].

Equation (2), which describes $H_{c2}(T)$ at all temperatures, simplifies close to T_c where it reduces to Eq. (1) with

$$H_{\mathrm{o}}=\frac{48\pi\phi_0k_B^2T_c^2}{7\zeta(3)\hbar^2[v_1^2+v_2^2+(v_1^2-v_2^2)\lambda_-/w]} \tag{6}$$

$$H_p=\frac{2\pi k_BT_c}{\mu\sqrt{7\zeta(3)}} \tag{7}$$

where $\zeta(3)\approx 1.202$. The slope $H_{c2}'=|dH_{c2}/dT|$ is maximum at T_c where Eqs. (2) and (6) yield

$$H_{c2}'=\frac{24\pi\phi_0k_B^2T_c}{7\zeta(3)\hbar^2(c_+v_1^2+c_-v_2^2)} \tag{8}$$

For identical bands, ($v_1=v_2=v$, $\lambda_{11}=\lambda_{22}$, $c_+=c_-=1/2$), Eq. (8) reduces to the single-band GL expression, $H_{c2}'=\phi_0/2\pi T_c\xi_0^2$, where $\xi_0=(\hbar v/\pi k_BT_c)[7\zeta(3)/48]^{1/2}$ is the GL coherence length in the clean limit [29]. For the $s^{\pm}$ pairing ($c_+\to c_-\to 1/2$), the dependence of H_{c2}' on the materials parameters resembles the behavior of $H_{c2}(T)$ in the s^{++} dirty limit: for strong band asymmetry ($\eta\ll 1$ or $\eta\gg 1$), H_{c2} in Eq. (8) is limited by the band with *larger* Fermi velocity, similar to H_{c2} mostly limited by the band with larger diffusivity for the s^{++} case [23]. Paramagnetic effects decrease the slope of H_{c2}' and reduce the effect of band asymmetry.

Figure 10 shows the fit of the measured $H_{c2}(T)$ to Eq. (2) for $H\|ab$. For this field orientation, the resistive transitions in Fig. 7 (c) are considerably sharper than for $H\|c$. This allowed us to clearly define the middle point of the resistive transition for the traces taken at lower temperatures, increasing the number of the H_{c2} data points. For the sake of simplicity, we consider here the case of $\epsilon_1=\epsilon_2=\epsilon$ for which $\gamma=\epsilon^{-1/2}$, and H_{ab} is defined by Eqs. (2) and (3) with rescaled $q\to q\epsilon^{-3/4}$, $\alpha\to\alpha\epsilon^{-1/2}$ and $\sqrt{b}\to\epsilon^{1/4}\sqrt{b}$ in G_1 and $\sqrt{\eta b}\to\epsilon^{1/4}\sqrt{\eta b}$ in G_2 [29]. The fit in Fig. 10 was done for $s^{\pm}$ pairing with $\lambda_{11}=\lambda_{22}=0$, $\lambda_{12}\lambda_{21}=0.25$, $\eta=0.9$, $H\|ab$, $\alpha=2.3$. Equation (2) describes $H_{c2}^c(T)$, $H_{c2}^{ab}(T)$ and $\gamma_H(T)=b_\|(T)/\sqrt{\epsilon}b_\perp(T)$ where $b_\|(T)$ is the solutions of Eq. (2) for $H\|c$ very well.

To see if the observed values of H_{c2}' are at least qualitatively consistent with Eq. (8) and the materials parameters of chalcogenides, we use the ARPES data [43–45] which give $E_F\simeq 20-50$ meV. Taking $E_F=30$ meV in Eq. (8) yields $H_{c2}'^{ab}$ [T/K] $\simeq 0.64\gamma(m/m_0)$, so the observed $H_{c2}'^{ab}=H_o^{ab}/T_c=31.4$ T/K and $\gamma=H_o^{ab}/H_o^c\approx 2.75$ corresponds to the value of $m\simeq 15m_0$ consistent with the ARPES data of $m/m_0=$ 3-20 for different FS pockets [43]. These estimates show that the paramagnetic effects for Fe-11 chalcogenides are indeed essential, and the parameter $\alpha^{ab}=\gamma\alpha$ defined by Eq. (4) is greater than 1. For $E_F=30$ meV and $T_c=14$ K, we obtain $\alpha^{ab}\simeq 0.13\gamma m/m_0$, giving $\alpha^{ab}\sim 5$. The values of $\alpha>1$ indicate that paramagnetic pair-breaking becomes so strong that it can trigger the FFLO instability at lower temperatures.

As follows from the results shown in Fig. 10, the anisotropy parameter $\gamma_H(T)$ decreases as T decreases. This behavior reflects the significant role of the Zeeman pair-breaking in FeSeTe given that $\alpha_\|=\alpha/\sqrt{\epsilon}=2.3$ for $H\perp c$ is well above the single-band FFLO instability threshold, $\alpha\approx 1$ [29]. In this case $\gamma_H(T)$ near T_c is determined by the orbital pairbreaking and the mass anisotropy ϵ, but as T decreases, the contribution of the isotropic Zeeman pairbreaking increases, resulting in the decrease of $\gamma_H(T)$.

The fit to our experimental data based on the solution of Eq. (2) predicts the FFLO transition for $H\|ab$. In this case Fig. 10 shows that the FFLO wave vector $Q(T)$ appears spontaneously at $T<T_F\approx 0.35T_c\approx 5$K, corresponding in optimally doped samples to magnetic fields $H\gtrsim 42$ T. Here $Q(T)$ increases from zero at $T=T_F$ to the maximum Q_0 at $T=0$, where $Q_0=4\pi T_cb(0)^{1/2}/\hbar v_1$. In addition to the strong Pauli pairbreaking $\alpha>1$, the

FFLO transition requires weak impurity scattering in the clean limit $\ell \gg \xi$ where ℓ is the mean free path due to elastic scattering on impurities [25]. The latter condition is likely satisfied in the crystals studied in this work, given the very short coherence lengths $\xi_{ab} \sim 14$ Å and $\xi_c \sim 5$ Å extracted from the fit described above. Thus, the chalcogenides are very good candidates to study the FFLO transition by magneto-transport, specific heat, magnetic torque or NMR measurements.

ANALYSIS OF THE CRITICAL REGION

Recent heat-capacity measurements on $\mathrm{FeSe_{0.5}Te_{0.5}}$ under field [36] found that it strongly resembles behavior previously observed in the much more anisotropic high-T_c cuprates, where strong fluctuation effects have been found to wipe out the phase transition at H_{c2}. In $\mathrm{FeSe_{0.5}Te_{0.5}}$ these fluctuations were found to be strongly anisotropic [36]. Here, we proceed to study the critical regime preceding the superconducting transition in our annealed BRST-grown single-crystals. In the critical region of the metal to superconducting transition, and in the limit of strong magnetic fields, one expects a scaling form for the thermodynamic functions. At very high fields if the quasiparticles are confined within the lowest Landau level, the transport of charge carriers becomes nearly one-dimensional along the direction of the applied field. Fluctuation effects close to the superconducting transition are expected to be enhanced by the lower effective dimensionality of the system. In the critical regime the fluctuation conductivity was calculated in Ref. 37 by including a quartic term in the free energy within the Hartree approximation, and obtained a scaling law for the fluctuation conductivity $\Delta\sigma$ in magnetic fields, in terms of unspecified scaling functions F_{2D} and F_{3D}, valid for two-dimensional and three-dimensional superconductors, [37] respectively:

$$\Delta\sigma(H)_{\mathrm{2D}} = \left(\frac{T}{H}\right)^{1/2} F_{\mathrm{2D}}\left(\alpha\frac{T-T_c(H)}{\sqrt{TH}}\right), \tag{9}$$

$$\Delta\sigma(H)_{\mathrm{3D}} = \left(\frac{T^2}{H}\right)^{1/3} F_{\mathrm{3D}}\left(\beta\frac{T-T_c(H)}{(TH)^{2/3}}\right), \tag{10}$$

Where α and β are characteristic constants of a specific material. Presumably, these functionals remain valid even if the quasiparticles are not confined to just the lowest Landau level, but are placed in a few higher Landau levels, as long as the interaction between quasiparticles in distinct Landau levels remains negligible. [38, 39] In the cuprates, either type of scaling has been observed in materials having distinct degrees of electronic/superconducting anisotropies. [40]

We define the contribution of the fluctuations to the conductivity $\Delta\sigma$ as the difference between the normal state conductivity $\sigma_n = 1/\rho_n$ (ρ_n is the normal state resistivity) and the measured conductivity $\sigma = 1/\rho$. Here σ_n is obtained from a polynomial fit of the resistivity in a temperature interval $\Delta T \sim 2T_c$ above T_c, where the contribution of the fluctuations to σ should become negligible. Here, T_c is defined as the middle point of the resistive transition, or the 50 %

In the left panel of Fig. 11, we plot $\Delta\sigma(H/T)^{1/2}$ versus $[T - T_c(H)]/(TH)^{1/2}$ for the annealed BRST single-crystal for both field orientations, as expected for the two-dimensional scaling relation in Eq. (9). For fields above a relatively small value of just 4 T, and for both orientations, this two-dimensional scaling clearly succeeds in collapsing all the curves over an extended temperature range particularly above T_c. We checked that this statement is still valid if the onset of the resistive transition (90 % of the resistance of the normal state) is used as the criteria to define T_c. Given that the high field resistive transitions shown in Fig. 7 are remarkably broad, it is not possible to unambiguously define the functional form of $\rho_n(H)$ in order to also collapse those curves in Fig. 11. To compare this two-dimensional scaling relation with the three-dimensional one, in the right panel of Fig. 11, we plot $\Delta\sigma H^{1/3}/T^{2/3}$ versus $[T - T_c(H)]/(TH)^{2/3}$ as expected for the three-dimensional case described by Eq. (10). Clearly, the two-dimensional relationship provides a better scaling of the data both above and below T_c. Indeed, in the three-dimensional case, the curves at different fields open like a fan above T_c and also tend to separate from each other below this critical temperature. On the other hand, in the 2D case, the curves above 4 T basically overlap over the entire range. The 2D behavior of fluctuation conductivity, already observed in the Fe arsenides, [41, 42] implies that the inter-plane coherence length ξ_c is smaller or in the order of the inter-plane spacing as found above, or, equivalently, that the coupling between adjacent superconducting planes is smaller than the intra-plane condensation energy. Notice, that our scaling analysis is consistent with the report of very anisotropic superconducting fluctuations according to heat capacity measurements [36]. Two-dimensional scaling also suggests that such fluctuations contribute to the broad transitions seen in Fig. 7, which become considerably sharper at lower temperatures.

DISCUSSION

There are several puzzling aspects in the $\mathrm{Fe_{1+y}Te_{1-x}Se_x}$ family that have yet to be understood and/or conciliated. For instance, optical spectroscopy measurements in $\mathrm{Fe_{1.06}Te_{0.88}S_{0.14}}$ indicates the absence of a Drude peak in optical conductivity, suggesting the absence of well-defined coherent quasi-particles in this material [46]. Although, for $\mathrm{FeSe_{0.42}Te_{0.58}}$ the in-plane optical conductivity is found to be indeed

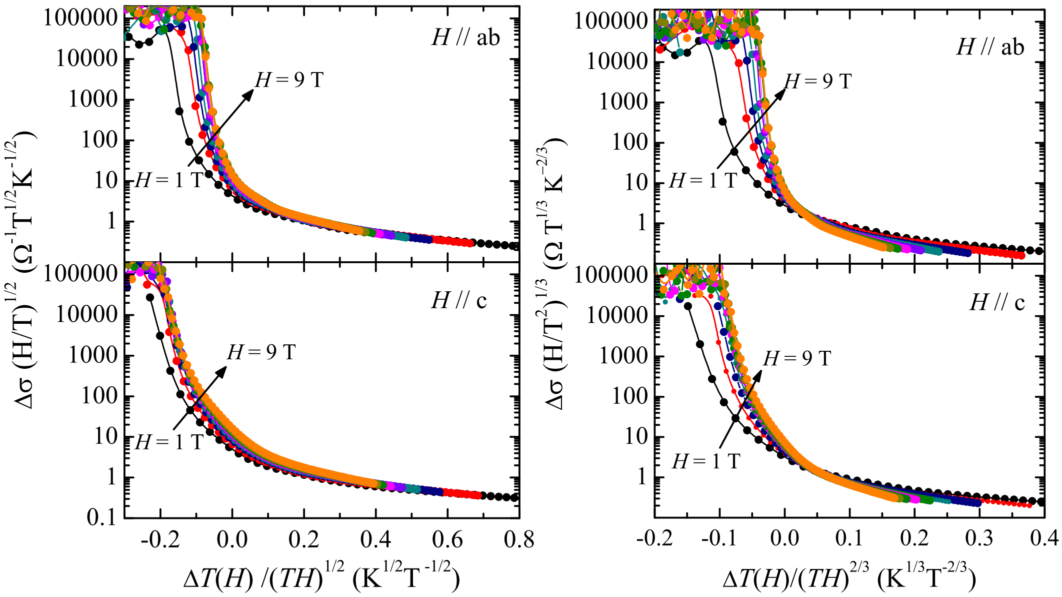

FIG. 11. (color online) Left panel: $\Delta\sigma(H/T)^{1/2}$ versus $\Delta T(H)/(TH)^{1/2}$ for the annealed BRST single-crystal and for both field orientations, as expected for the two-dimensional scaling relation of Eq. (2). Here, $\Delta\sigma = (1/\rho - 1/\rho_n)$ where $1/\rho$ is the resistivity across the superconducting transition and $1/\rho_n$ is the resistivity in the normal state preceding the transition (see main text), while $\Delta T(H) = [T - T_c(H)]$. Right Panel: $\Delta\sigma H^{1/3}/T^{2/3}$ versus $[T - T_c(H)]/(TH)^{2/3}$ as expected for the three-dimensional scaling relation in Eq. (3).

describable within a Drude-Lorentz model [47] but with an incoherent response along the inter-planar direction [48]. Therefore, one could even ask if the concept of Fermi surface would be applicable to these compounds. In sharp contrast, a recent angle resolved photoemission study on $\mathrm{FeSe}_{0.42}\mathrm{Te}_{0.58}$ [49] reveals a Fermi surface which is in relative good qualitative agreement with the generic Fermi surface proposed for the family of Fe pnictides. Namely, composed by two concentric hole-like cylindrical surfaces at the Γ point and two electron-like cylinders at the M point of the Brillouin zone, which are characterized by a large, FS-sheet dependent, effective-mass enhancement. This indicates that correlations are particularly relevant for these materials which is consistent with the size of the anomaly observed in the heat capacity at the superconducting transition [50] or the large H_{c2} reported here and by other groups [20, 24, 33]. This geometry would be consistent with the observation of a resonance mode characterized by a wave-vector connecting both types of cylindrical Fermi surfaces [12] pointing towards an itinerant, nesting-like mechanism for the origin of the spin-fluctuations in these systems. Although, this scenario seems difficult to conciliate with the rather large magnetic moment of 1.6 to 1.8 μ_B for the non-interstitial Fe(I) ion as extracted from careful magnetic susceptibility measurements in *superconducting* samples [51], and does not explain the observation of short-range magnetic-order in (superconducting samples) for the same wave-vector as the one extracted for the magnetically ordered state of $\mathrm{Fe}_{1+y}\mathrm{Te}$ [6]. The interstitial Fe(II) is presumably characterized by an even larger moment of $\sim 2.5\ \mu_B$ [6, 51] and from the superconducting perspective it should act as a magnetic impurity.

A recent DFT + DMFT study suggests that a combination of Hund's rule and structural degrees of freedom, such as the pnictogen height and the bond angle between Fe and the pnictide element, are the key parameters defining the role of correlations, i.e. the degree of localization and therefore the concomitant size of the magnetic moment of Fe in iron pnictide compounds [52]. For instance, the larger the size of the pnictogen atom or equivalently the larger the distance between Fe and this element, or the greater the deviation with respect to the ideal tetrahedral angle of 109.5°, the larger the degree of localization in the Fe site. Or equivalently, the stronger the correlations on those Fermi surface sheets having a marked t_{2g} character which would favor the development of a magnetic instability. It is therefore easy to speculate on the role played by the interstitial Fe(II): it should favor local lattice distortions that are likely to further distort the Fe-pnictogen angle away from 109.5° favoring local magnetism in detriment of superconductivity. The larger the content in Fe(II) the stronger this detrimental effect, while larger fluctuations in y could create randomly distributed nearly magnetic patches having a stronger Fe(II) content which could lead to pair-breaking effects. This rather simple scenario would explain why the annealed BRST-grown samples display clearer and sharper superconducting transitions when compared to the non-annealed ones despite a similarly poor crystallinity.

As for the presence of the FFLO state [25], it is presumably sensitive to impurities being difficult to conciliate with the presence of magnetic Fe(II) atoms. However, our results suggest that our BRST-grown samples (annealed as well as non-annealed) are closer to having a nearly stoichiometric Fe content. Furthermore, the low-T upturn in $H_{c2}^{c}(T)$ indicative of the FFLO instability as observed in this work, was also observed by other groups, see for example, Ref. 24. Finally, the interplay between magnetism and the FFLO-state is still poorly understood [53], so its existence in the $\mathrm{Fe}_{1+y}\mathrm{Te}_{1-x}\mathrm{Se}_x$ will only be clarified by future calorimetric, magnetic torque or NMR measurements at high fields.

Finally, given that the inter-plane coherence length ξ_c is in the order of the inter-planar distance it is relatively easy to understand why the mosaic spread associated with relative orientation among Fe[Se,Te] planes has little effect on the superconducting properties of these materials. Although the superconducting anisotropy is small, the size of ξ_c implies that the Cooper pairs are virtually localized within the planes thus remaining almost oblivious to the potential pair-breaking effects imposed by the grain boundaries located between the planes.

CONCLUSION

In conclusion, we find that the Fe[Te,Se] planes are well stacked along the c-axis, forming domains with well aligned planes spanning a certain coherence length along the c-axis. These domains display a small twist to each other, in the order of a degree or less relative, defining grain boundaries. Our study strongly indicates that these domain boundaries have little or no effect on the superconducting properties of the $\mathrm{Fe}_{1+y}\mathrm{Te}_{1-x}\mathrm{Se}_x$ series. However, a relatively weak disorder in the distribution of interstitial Fe is found to be detrimental to the superconducting properties of the $\mathrm{Fe}_{1+y}\mathrm{Te}_{1-x}\mathrm{Se}_x$ series, broadening the width of the superconducting transition and suppressing the diamagnetic response. We attribute this to local lattice distortions associated with the interstitial Fe(II) which are likely to locally increase the electronic correlations leading to a higher degree of carrier localization favoring magnetism in detriment of superconductivity. In samples displaying the sharpest superconducting transitions and a very clear diamagnetic signal, we observe a mild upturn in the upper critical field at lower temperatures consistent with the Fulde-Ferrel-Larkin-Ovchinnikov instability. These samples display metallic resistivity suggesting also the formation of coherent quasi-particles at lower temperatures in contrast to previous reports [46], and implying that a relatively mild excess of randomly distributed Fe(II) atoms may be enough to suppress the phase coherence. Finally, our estimates of the inter-plane coherence length $\xi_c \sim 5.1 < 6$ Å where $c \simeq 6$ Å is the inter-planar lattice constant, is consistent with the quasi-two-dimensional superconducting fluctuations in the critical region (also observed by other groups[41, 42]).

ACKNOWLEDGEMENTS

The NHMFL is supported by NSF through NSF-DMR-0084173 and the State of Florida. L. B. is supported by DOE-BES through award de-sc0002613. JW, TG and TS acknowledge support from FSU.

---

[*] balicas@magnet.fsu.edu

[1] F. C. Hsu, J. Y. Luo, K. W. Yeh, T. K. Chen, T. W. Huang, P. M. Wu, Y. C. Lee, Y. L. Huang, Y. Y. Chu, D. C. Yan, and M. K. Wu, Proc. Natl. Acad. Sci. U.S.A. **105**, 14262 (2008).

[2] M. H. Fang, H. M. Pham, B. Qian, T. J. Liu, E. K. Vehstedt, Y. Liu, L. Spinu, and Z. Q. Mao, Phys. Rev. B **78**, 224503 (2008).

[3] K. W. Yeh, T. W. Huang, Y. L. Huang, T. K. Chen, F. C. Hsu, P. M. Wu, Y. C. Lee, Y. Y. Chu, C. L. Chen, J. Y. Luo, D. C. Yan, and M. K. Wu, EPL **84**, 37002 (2008).

[4] Y. Mizuguchi, F. Tomioka, S. Tsuda, T. Yamaguchi, and Y. Takano, Appl. Phys. Lett. **93**, 152505 (2008); S. Margadonna, Y. Takabayashi, Y. Ohishi, Y. Mizuguchi, Y. Takano, T. Kagayama, T. Nakagawa, M. Takata, and K. Prassides, Phys. Rev. B **80**, 064506 (2009); G. Garbarino, A. Sow, P. Lejay, A. Sulpice, P. Toulemonde, M. Mezouar, and M. Nunez-Regueiro, Europhys. Lett. **86**, 27001 (2009); S. Medvedev, T. M. McQueen, I. A. Troyan, T. Palasyuk, M. I. Eremets, R. J. Cava, S. Naghavi, F. Casper, V. Ksenofontov, G. Wortmann and C. Felser, Nat. Mater. **8**, 630 (2010).

[5] D. Fruchart, P. Convert, P. Wolfers, R. Madar, J. P. Senateur, and R. Fruchart, Mater. Res. Bull. **10**, 169 (1975).

[6] W. Bao, Y. Qiu, Q. Huang, M. A. Green, P. Zajdel, M. R. Fitzsimmons, M. Zhernenkov, S. Chang, M. Fang, B. Qian, E. K. Vehstedt, J. Yang, H. M. Pham, L. Spinu, and Z. Q. Mao, Phys. Rev. Lett. **102**, 247001 (2009).

[7] S. L. Li, C. de la Cruz, Q. Huang, Y. Chen, J. W. Lynn, J. P. Hu, Y. L. Huang, F. C. Hsu, K. W. Yeh, M. K. Wu, and P. C. Dai, Phys. Rev. B **79**, 054503 (2009).

[8] C. de la Cruz, Q. Huang, J. W. Lynn, J. Li, W. R. Ii, J. L. Zarestky, H. A. Mook, G. F. Chen, J. L. Luo, N. L. Wang, and P. C. Dai, Nature (London) **453**, 899 (2008).

[9] Q. Huang, Y. Qiu, W. Bao, M. A. Green, J. W. Lynn, Y. C. Gasparovic, T. Wu, G. Wu, and X. H. Chen, Phys. Revs. Lett. **101**, 257003 (2008).

[10] J. Zhao, D. -X. Yao, S. Li, T. Hong, Y. Chen, S. Chang, W. Ratcliff II, J. W. Lynn, H. A. Mook, G. F. Chen, J. L. Luo, N. L. Wang, E. W. Carlson, J. Hu, and P. C. Dai, Phys. Rev. Lett. **101**, 167203 (2008).

[11] A. Subedi, L. J. Zhang, D. J. Singh, and M. H. Du, Phys. Rev. B **78**, 134514 (2008).

[12] Y. M. Qiu, W. Bao, Y. Zhao, C. Broholm, V. Stanev, Z. Tesanovic, Y. C. Gasparovic, S. Chang, J. Hu, B. Qian, M. H. Fang, and Z. Q. Mao, Phys. Rev. Lett. **103**, 067008 (2009).

[13] T. Imai, K. Ahilan, F. L. Ning, T. M. McQueen, and R. J. Cava, Phys. Rev. Lett. **102**, 177005 (2009).

[14] Y. Xia, D. Qian, L. Wray, D. Hsieh, G. F. Chen, J. L. Luo, N. L. Wang, and M. Z. Hasan, Phys. Rev. Lett. **103**, 037002 (2009).

[15] K. Nakayama, T. Sato, P. Richard, T. Kawahara, Y. Sekiba, T. Qian, G. F. Chen, J. L. Luo, N. L. Wang, H. Ding, and T. Takahashi, Phys. Rev. Lett. **105**, 197001 (2010).

[16] B. Zeng, G. Mu, H. Q. Luo, T. Xiang, H. Yang, L. Shan, C. Ren, I. I. Mazin, P. C. Dai, and H. -H. Wen, Nat. Commun. **1**, 112 (2010).

[17] T. M. McQueen, Q. Huang, V. Ksenofontov, C. Felser, Q. Xu, H. Zandbergen, Y. S. Hor, J. Allred, A. J. Williams, D. Qu, J. Checkelsky, N. P. Ong, and R. J. Cava, Phys. Rev. B **79**, 014522 (2009).

[18] T. J. Liu, X. Ke, B. Qian, J. Hu, D. Fobes, E. K. Vehstedt, H. Pham, J. H. Yang, M. H. Fang, L. Spinu, P. Schiffer, Y. Liu, and Z. Q. Mao, Phys. Rev. B **80**, 174509 (2009).

[19] H. Lei, R. Hu, E. S. Choi, J. B. Warren, and C. Petrovic, Phys. Rev. B **81**, 094518 (2010).

[20] M. Fang, J. Yang, F. F. Balakirev, Y. Kohama, J. Singleton, B. Qian, Z. Q. Mao, H. Wang, and H. Q. Yuan, Phys. Rev. B **81**, 020509(R) (2010).

[21] L. Lyard, P. Samuely, P. Szabo, C. Marcenat, T. Klein, K. H. P. Kim, C. U. Jung, H. -S. Lee, B. Kang, S. Choi, S. -I. Lee, L. Paulius, J. Marcus, S. Blanchard, A. G. M. Jansen, U Welp, G. Karapetrov and W. K. Kwok, Supercond. Sci. Technol. **16**, 193 (2003).

[22] A. Gurevich, S. Patnaik, V. Braccini, K. H. Kim, C. Mielke, X. Song, L. D. Cooley, S. D. Bu, D. M. Kim, J. H. Choi, L. J. Belenky, J. Giencke, M. K. Lee, W. Tian, X. Q. Pan, A. Siri, E. E. Hellstrom, C. B. Eom and D. C. Larbalestier, Supercond. Sci. Technol. **17**, 278 (2004).

[23] A. Gurevich, Phys. Rev. B **67**, 184515 (2003); Physica C **456**, 160 (2007).

[24] S. Khim, J. W. Kim, E. S. Choi, Y. Bang, M. Nohara, H. Takagi, and K. H. Kim, Phys. Rev. B **81**, 184511 (2010).

[25] P. Fulde and R. A. Ferrell, Phys. Rev. **135**, A550 (1964); A. I. Larkin and Yu. N. Ovchinnikov, Sov. Phys. JETP **20**, 762 (1965). Y. Matsuda and H. Shimahara, J. Phys. Soc. Jpn. **76**, 051005 (2007).

[26] Y. Liu and C. T. Lin, J. Supercond. Nov. Magn. **24**, 183 (2011).

[27] Y. Mizuguchi and Y. Takano, J. Phys. Soc. Jpn. **79**, 102001 (2010).

[28] B. C. Sales, A. S. Sefat, M. A. McGuire, R. Y. Jin, D. Mandrus, Y. Mozharivskyj, Phys. Rev. B **79**, 094521 (2009).

[29] A. Gurevich, Phys. Rev. B **82**, 184504 (2010).

[30] The detailed crystallographic information file (CIF) for a typical TSFZ single crystal x-ray refinement with CSD # 423463 is available at: http://www.fiz-karlsruhe.de.

[31] J. Yang, M. Matsui, M. Kawa, H. Ohta, C. Michioka, C. Dong, H. Wang, H. Yuan, M. Fang and K. Yoshimura, J. Phys. Soc. Jpn. **79**, 074704 (2010).

[32] See supplemental material at http://link.aps.org/supplemental/

[33] T. Klein, D. Braithwaite, A. Demuer, W. Knafo, G. Lapertot, C. Marcenat, P. Rodière, I. Sheikin, P. Strobel, A. Sulpice, and P. Toulemonde, Phys. Rev. B **82**, 184506 (2010).

[34] M. Tegel, C. Löhnert, and D. Johrendt, Solid State Commun. **150**, 383 (2010).

[35] J. Jaroszynski, S. C. Riggs, F. Hunte, A. Gurevich, D. C. Larbalestier, G. S. Boebinger, F. F. Balakirev, A. Migliori, Z. A. Ren, W. Lu, J. Yang, X. L. Shen, X. L. Dong, Z. X. Zha, R. Jin, A. S. Sefat, M. A. McGuire, B. C. Sales, D. K. Christen, and D. Mandrus, Phys. Rev. B **78**, 064511 (2008).

[36] A. Serafin, A. I. Coldea, A. Y. Ganin, M. J. Rosseinsky, K. Prassides, D. Vignolles, and A. Carrington, Phys. Rev. B **82**, 104514 (2010).

[37] S. Ullah and A. T. Dorsey, Phys. Rev. Lett. **65**, 2066 (1990); S. Ullah and A. T. Dorsey, Phys. Rev. B **44**, 262 (1991).

[38] Z. Tešanovic and A. V. Andreev, Phys. Rev. B **49**, 4064 (1994).

[39] Z. Tešanovic, L. Xing, L. Bulaevskii, Q. Li, and M. Suenaga, Phys. Rev. Lett. **69**, 3563 (1992).

[40] M. Roulin, A. Junod, and E. Walker, Physica C **260**, 257 (1996); D. H. Kim, K. E. Gray, and M. D. Trochet, Phys. Rev. B **45**, 10801 (1992); U. Welp, S. Fleshler, W. K. Kwok, R. A. Klemm, V. M. Vinokur, J. Downey, B. Veal, and G. W. Crabtree, Phys. Rev. Lett. **67**, 3180 (1991); N. Overend, M. A. Howson, I. D. Lawrie, S. Abell, P. J. Hirst, C. Changkang, S. Chowdhury, J. W. Hodby, S. E. Inderhees, and M. B. Salamon, Phys. Rev. B **54**, 9499 (1996); M. Costa, P. Pureur, L. Ghivelder, J. A. Campá, and I. Rasines, Phys. Rev. B **56**, 10836 (1997); S. W. Pierson, T. M. Katona, Z. Tešanovic, and O. T. Valls, Phys. Rev. B **53**, 8638 (1996); M. Costa, P. Pureur, M. Gusmão, S. Senoussi, and K. Behnia, Phys. Rev. B **64**, 214513 (2001).

[41] I. Pallecchi, C. Fanciulli, M. Tropeano, A. Palenzona, M. Ferretti, A. Malagoli, A. Martinelli, I. Sheikin, M. Putti, and C. Ferdeghini, Phys. Rev. B **79**, 104515 (2009).

[42] M. Putti, I. Pallecchi, E. Bellinger, M. Tropeano, C. Ferdeghini, A. Palenzona, C. Tarantini, A. Yamamoto, J. Jiang, J. Jaroszysnki, F. Kametani, D. Abraimov, A. Polyanskii, J. D. Weiss, E. E. Hellstrom, A. Gurevich, D. C. Larbalestier, R. Jin, B. C. Sales, A. S. Sefat, M. A. McGuire, D. Mandrus, P. Cheng, Y. Jia, H. H. Wen, S. Lee, and C. B. Eom, Supercond. Sci. Technol. 2**3**, 034003 (2010).

[43] K. Nakayama, T. Sato, P. Richard, T. Kawahara, Y. Sekiba, T. Qian, G. F. Chen, J. L. Luo, N. L. Wang, H. Ding, and T. Takahashi, Phys. Rev. Lett. **105** 197001 (2010)

[44] F. Chen, B. Zhou, Y. Zhang, J. Wei, H.W. Ou, J.F. Zhao, C. He, Q.Q. Ge, M. Arita, K. Shimada, H. Namatame, M. Taniguchi, Z.-Y. Lu, J. Hu, X.-Y. Cui, and D. L. Feng Phys. Rev. B **81**, 014526 (2010).

[45] A. Tamai, A. Y. Ganin, E. Rozbicki, J. Bacsa, W. Meevasana, P. D. C. King, M. Caffio, R. Schaub, S. Margadonna, K. Prassides, M. J. Rosseinsky, and F. Baumberger, Phys. Rev. Lett. **104** 097002 (2010).

[46] N. Stojilovic, A. Koncz, L. W. Kohlman, Rongwei Hu, C. Petrovic, and S. V. Dordevic, Phys. Rev. B **81**, 174518 (2010).

[47] C. C. Homes, A. Akrap, J. S. Wen, Z. J. Xu, Z. W. Lin, Q. Li, and G. D. Gu, Phys. Rev. B **81**, 180508 (2010).

[48] S. J. Moon, C. C. Homes, A. Akrap, Z. J. Xu, J. S. Wen, Z. W. Lin, Q. Li, G. D. Gu, and D. N. Basov, Phys. Rev. Lett. **106**, 217001 (2011).

[49] A. Tamai, A. Y. Ganin, E. Rozbicki, J. Bacsa, W. Meevasana, P. D. C. King, M. Caffio, R. Schaub, S. Margadonna, K. Prassides, M. J. Rosseinsky, and F. Baumberger, Phys. Rev. Lett. **104**, 097002 (2010).

[50] J. Hu, T. J. Liu, B. Qian, A. Rotaru, L. Spinu, and Z. Q. Mao, Phys. Rev. B **83**, 134521 (2011).

[51] J. Yang, M. Matsu, M. Kawa, H. Ohta, C. Michioka, C. Dong, H. Wang, H. Yuan, M. Fang, and K. Yoshimura, J. Phys. Soc. Jpn. **79**, 074704 (2010).

[52] Z. P. Yin, K. Haule, and G. Kotliar, arXiv:1104.3454v1 (2011).

[53] M. Kenzelmann, T. Strassle, C. Niedermayer, M. Sigrist, B. Padmanabhan, M. Zolliker, A. D. Bianchi, R. Movshovich, E. D. Bauer, J. L. Sarrao, J. D. Thompson, Science **321**, 1652 (2008).